ELSEVIER

Polymer 41 (2000) 2937–2945

polymer

The structure of poly(cyano-*p*-xylylene)

S.-Y. Park[a], J. Blackwell[a,*], S.N. Chvalun[a,b], A.A. Nikolaev[b], K.A. Mailyan[b], A.V. Pebalk[b], I.E. Kardash[b]

[a]*Department of Macromolecular Science, Case Western Reserve University, Cleveland, OH 44106-7202, USA*
[b]*Karpov Institute of Physical Chemistry, Vorontzovo Pole 10, 103064 Moscow, Russia*

Received 22 July 1998; received in revised form 16 June 1999; accepted 22 June 1999

Abstract

Films of poly(cyano-*p*-xylylene) (CN-PPX) synthesized by vapor deposition polymerization are highly crystalline and can be prepared with uni-planar orientation. This orientation is maintained after drawing the film 700% at 350°C, when the chains become aligned parallel to the direction of draw, leading to a mosaic texture of doubly-oriented crystals. Three-dimensional wide angle X-ray data show that the polymer has a monoclinic unit cell with dimensions $a = 5.96$ Å, $b = 13.52$ Å, $c = 6.48$ Å and $\beta = 135.9°$, containing two monomer units from symmetry related chains. The unit cell is almost identical to that of the α-form of the unsubstituted polymer, poly(*p*-xylylene), except for the increased *b* dimension ($b = 10.64$ Å in PPX), which is due to the –CN substituent. Molecular modeling and X-ray simulations show that the two polymers have similar crystal structures. The best agreement between the observed and calculated structure amplitudes ($R = 0.21$) is for a model where there is random substitution of the –CN groups.

Keywords: Poly(cyano-*p*-xylylene); Crystal structure; Molecular modeling

1. Introduction

Poly(*p*-xylylene) (PPX) and its derivatives have potential as interlayer dielectrics because of their high thermal and chemical stability, excellent mechanical properties, low dielectric constants, and the fact that they can be synthesized and processed as thin coatings by vapor deposition [1]. The fluorine-containing derivative of PPX, poly(α,α,α′,α′-tetrafluoro-*p*-xylylene) (PPX-F) is especially promising, in that it combines a low dielectric constant (~2.2) and high thermal stability (up to 530°C, compared to ~315°C for α-PPX) [2–7]. The thermo-oxidative stability of PPX can also be increased by substituting electron-acceptor groups on the phenyl rings, such as in poly(chloro-*p*-xylylene) (Cl-PPX) and poly(cyano-*p*-xylylene) (CN-PPX) which are stable up to ~430°C [8]. The dielectric constants of Cl-PPX (3.1) and CN-PPX (3.4) are higher than that of PPX (2.7), but they are still lower than that of conventional interlayer dielectric, SiO_2 (~3.9).

The crystal structure of PPX was studied by Brown and Farhing [9], who reported the existence of two polymorphic forms, designated α- and β-PPX. X-ray and electron diffraction studies by Wunderlich and coworkers [10,11] showed that α-PPX has a monoclinic unit cell with dimensions $a = 5.92$ Å, $b = 10.64$ Å, $c = 6.55$ Å (chain axis) and $\beta = 134.7°$; the space group is $C2/m$, and the cell contains two monomer units. The proposed chain conformation has all-*trans* $-CH_2-CH_2-$ groups inclined at 90° to the adjacent phenyl groups. Isoda et al. [12] reported a more complex structure for the β-form: this has a large trigonal unit cell containing 16 monomers, with dimensions $a = b = 20.52$ Å, and $c = 6.55$ Å, and space group $P3$. Recently, we found that PPX-F adopts a triclinic unit cell with dimensions $a = 5.36$ Å, $b = 5.92$ Å, $c = 6.57$ Å (chain axis repeat), $\alpha = 97.0°$, $\beta = 63.1°$, and $\gamma = 73.1°$, containing one monomer unit [4]. This structure is similar to that of α-PPX, except for dilation along the *a*-axis in order to accommodate fluorine atoms. For Cl-PPX, Isoda et al. [13] report a monoclinic unit cell with dimensions $a = 5.92$ Å, $b = 12.80$ Å, $c = 6.55$ Å, $\beta = 135.0°$. These dimensions are the same as those for α-PPX, except for the larger *a* dimension, but no information is available with regard to the arrangement of the chlorine substituents.

In the work described below, we have used X-ray diffraction and molecular modeling to investigate the structure of CN-PPX, in order to compare it to the unsubstituted polymer (PPX), the chlorinated and fluorinated analogs (Cl-PPX and PPX-F).

* Corresponding author. Tel.: +1-216-368-6370; fax: +1-216-368-4202.
E-mail address: jxb6@po.cwru.edu (J. Blackwell).

0032-3861/00/$ - see front matter
PII: S0032-3861(99)00462-0

2. Experimental

2.1. Materials

CN-PPX was prepared from dicyano-[2,2]*para*-cyclophane according to the vapor deposition polymerization (VDP) scheme first reported by Yeh and Gorham [14]:

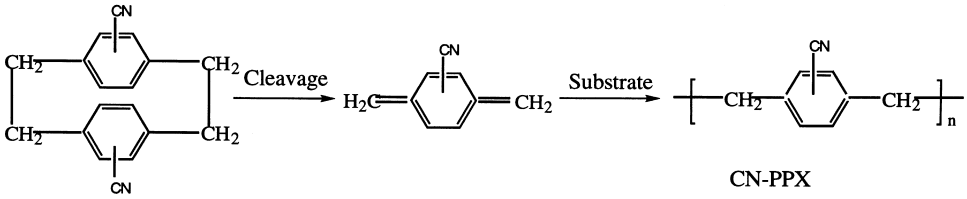

CN-PPX

Dicyano-[2,2]*para*-cyclophane was synthesized as described by Kardash and coworkers [8], and purified by sublimation in vacuo. The synthesis was carried out using VDP equipment similar to that described by Mailyan et al. [15]: sublimation at 130°C, pyrolysis at 650°C, and deposition on polished glass substrates at −35, −5, 20 or 40°C, at a pressure (before sublimation) of $\sim 5 \times 10^{-3}$mmHg. When peeled from the substrates, the resultant films were transparent, tough and 20–30 μm thick.

Solution of the film products in LiCl/*N*-methylpyrolidone at room temperature had intrinsic viscosities ranging from 2.85 to 8.3 dl/g for films deposited at −35 and 25°C, respectively, corresponding [16] to molecular weights of ~ 1.5–8.5×10^5 : these molecular weights are similar to those estimated for unsubstituted of PPX ~ 2–4×10^5 based on ESR data [1]. TGA analysis (in air at 10°C/min) showed high thermostability for CN-PPX films: 10% weight loss had occurred at 430°C.

To improve the crystalline order, the as-deposited samples were annealed for 30 min at 200°C, using a frame to prevent contraction. The films deposited at 40°C were drawn up to 700% at 350°C. The density was measured by flotation in a mixture of chloroform and dimethylsulfoxide, which are miscible non-solvents.

Wide angle X-ray diffraction patterns were recorded on Kodak Direct Exposure film, using Ni-filtered CuK_α radiation. Resolution of the *hkl* reflections in the three-dimensional (3D) scattering data was achieved using a Siemens Hi-Star® area detector. The film was arranged with the draw direction perpendicular to the beam, and tilted by the angle ω equal to the Bragg angle for each layer line, after which it was rotated through the angle ϕ in 10° increments about the draw direction ($\phi = 0°$ for ND direction). The rotation angle ϕ_t for the intensity maximum for each *hkl* reflection was determined by interpolation. The total intensity at successive points along each layer line was determined by (azimuthal) integration after the subtraction of the background scattering, and was corrected for differences in effective film thickness due to tilt and rotation as described by Alexander [17].

Additional wide angle data were recorded as $2\theta/\theta$ scans, using a Philips PN 3550/10 diffractometer operating in the transmission mode. The intensities of the Bragg reflections were measured from the peak areas in a diffractometer scan for an annealed isotropic specimen that had been prepared by deposition −35°C. After correction for the Lorentz and polarization effects, intensities were converted to structure amplitudes, $|F_o(hkl)|$. Note that these data contained 14 observed reflections, which are resolved into 17 reflections in the 3D data, collected using the area detector. The former were preferred for comparison with those predicted because it is difficult to normalize the intensities on different layer lines to form a single data set. The crystallographic *R*-value was determined as the normalized difference between the observed and calculated structural amplitudes. The latter were derived from the atomic coordinates of the models described below. The observed structure amplitudes for one peak assigned to two *hkl* reflections was compared to the square root of the sum of the square of calculated amplitudes, $(\sum F_c^2(hkl))^{1/2}$. In addition, 15 reflections that were predicted within the region of the observed data but were too weak to be observed were included in the $|F_o(hkl)|$ data by assigning intensities of half the threshold intensity. The packing fraction, the ratio of the van der Waals volume of the structure within the unit cell to the total volume, was calculated using the SYBYL® software package (Tripos Inc.).

2.2. Molecular modeling and X-ray simulation

Molecular mechanics modeling was performed using the SYBYL® package. Partial charges were calculated using the method of Gasteiger and Hückel. The potential energy was computed as the sum of the contribution due to van der Waals and electrostatic forces, distortions of the bond lengths, bond angles and torsion angles, and the effects of out-of-plane bending. The optimum bond angles and bond length were those of the SYBYL® force field. The chain conformation depends primarily on the torsion angles χ_1, χ_2 and χ_3 defined below:

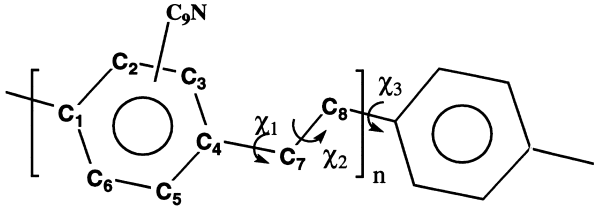

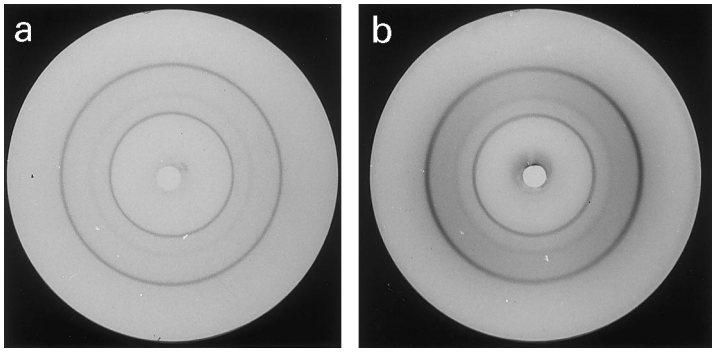

Fig. 1. Wide angle X-ray patterns of the as-deposited film of CN-PPX at −35°C. The X-ray beam was inclined (a) perpendicular to the film surface and (b) parallel to the film surface (the plane of film is vertical).

0° for each torsion angle corresponds to the *cis* position relative to the carbon atoms.

No information exists concerning the microstructure of CN-PPX, i.e. whether the –CN groups are substituted randomly or whether there is a preference for one or more certain positions on the phenylene ring. We therefore compared three basic models: in model 1, all the –CN groups are at the C2 position. In model 2, they are randomly disposed 50/50 at C2 and C3, but are physically always to one side of the molecule, i.e. they cannot be at C5 and C6. In model 3, we have completely random substitution, i.e. 25% at each of C2, C3, C5 and C6. The packing energies for 7 × 7 arrays of chains of methyl-terminated decamers were minimized for models constructed using the unit cell dimensions determined from the X-ray data. In each case, the starting chain conformation was $\chi_1 = 90°$, $\chi_2 = 180°$ and $\chi_3 = -90°$. The models were then compared in terms of the potential energies of the central seven chains, which eliminated most of the edge effects, notably small lateral contraction of the arrays.

The structure amplitudes ($|F_c(hkl)|$) for the proposed structure were calculated using the CERIUS® software package. The atomic coordinates were based on those for α-PPX, which has very similar chemical and physical structure. Random disposition of the –CN groups was treated by assigning fractional occupancies. However, such averaging is problematic, because the chain conformation depends on the local environment. For this reason, we also simulated the X-ray fiber patterns for models 1–3, both before and after energy minimization using the CERIUS® software. The hydrogen atoms were ignored for these simulations.

3. Results and discussion

3.1. X-ray diffraction

Fig. 1 shows the wide angle X-ray data for an annealed film of CN-PPX that had been deposited at −35°C. These data were recorded with the beam inclined (a) parallel and (b) perpendicular to the film surface. Both X-ray patterns consist of almost isotropic rings with the same *d*-spacings and relative intensities: the polymer is highly crystalline, and there is relatively little preferred orientation.

The equivalent data for a film deposited at 40°C are shown in Fig. 2. When the X-ray beam is perpendicular to the film surface (Fig. 2(a)), we observe a series of isotropic rings, but these are broken into arcs when the beam is parallel to the film surface (Fig. 2(b)), pointing to preferred orientation of the crystallites. The peaks are broader than those for the film deposited at −35°C, indicating a smaller crystallite size, which may be due to a higher molecular weight.

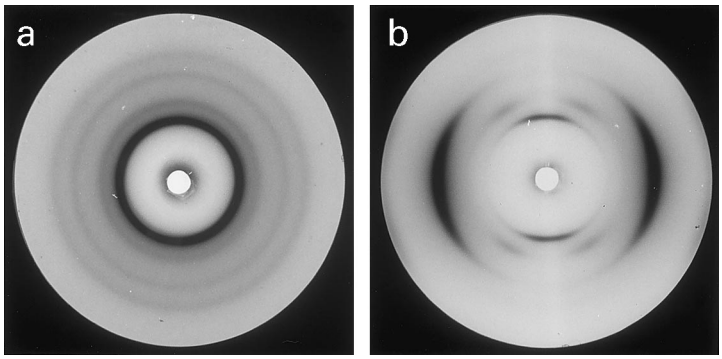

Fig. 2. Wide angle X-ray patterns of the as-deposited film of CN-PPX at 40°C. The X-ray beam was inclined (a) perpendicular to the film surface and (b) parallel to the film surface (the plane of film is vertical).

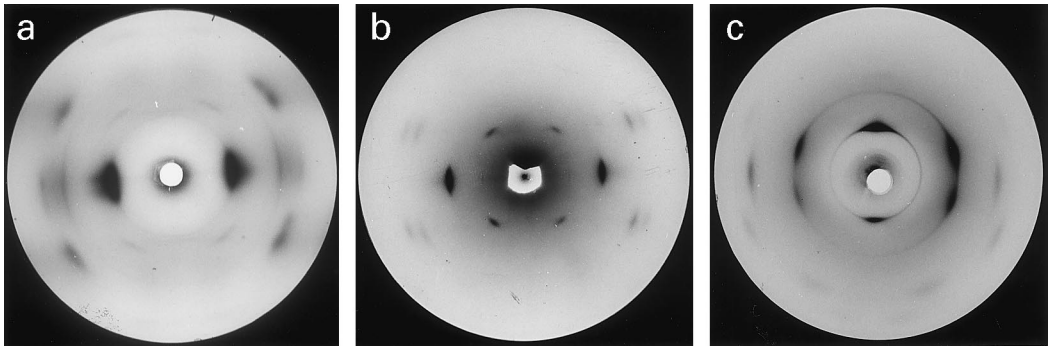

Fig. 3. Wide angle X-ray patterns of the drawn and annealed film of F-PPX. The X-ray beam was inclined (a) along the ND direction; (b) along the TD direction; and (c) along the OD direction.

There are also clear differences in relative intensities of the reflections in the two patterns: for example, the equatorial peak at $d \approx 4.0$ Å is very strong in Fig. 2(b), but it is weak in Fig. 2(a), indicating that it arises from lattice planes that are preferentially inclined parallel to the film surface. The strong Bragg peak at $d \approx 6.8$ Å is concentrated on the meridian in Fig. 2(b), and derives from lattice planes perpendicular to the film surface.

Fig. 3 shows the wide angle X-ray patterns of a film of CN-PPX that had been deposited at 40°C, drawn 700%, and annealed. The beam was aligned (a) normal to the film surface (the ND pattern), (b) perpendicular to both drawing and normal directions (the TD pattern), and (c) parallel to the draw direction (the OD pattern). Layer lines at orders of $c = 6.48 \pm 0.05$ Å are resolved perpendicular to the draw direction in the ND and TD patterns. This fiber repeat is shorter than that of PPX ($c = 6.55$ Å). The azimuthal scan of the equatorial reflection at $d = 6.76$ Å, has a half width of approximately 12.4°, indicating a high degree of axial orientation. In all, 17 Bragg reflections are observed, with d-spacings listed in Table 1. This compares with 35 reflections resolved in the equivalent data for PPX-F, which has a larger crystallite size in the doubly oriented film.

The data in Fig. 3 point to a highly oriented uni-planar texture. For example, the first equatorial peak at $d = 6.76$ Å is much stronger in the ND pattern than in the TD pattern. In contrast, the second equatorial peak at $d \approx 4.0$ Å is much stronger in the TD pattern than in the ND pattern. Thus, the

Table 1
Observed and calculated d-spacings, rotation angles and structure amplitudes for models 1–3

h	k	l	d_o	d_c	ϕ_o	ϕ_c[a]	F_o	F_c		
								Model 1	Model 2	Model 3
0	2	0	6.76	6.76	9	7(0)	7.2	8.7	9.0	9.8
1	1	0	3.96	3.96	79	84(73)	11.0	10.0	10.0	10.0
0	4	0	3.38	3.38	14	13(0)	2.1	1.8	2.0	2.2
1	3	0	3.07	3.05	57	62(47)	1.7	1.9	1.8	1.7
2	0	0	2.09	2.07	90	90(90)	1.5	1.6	1.5	1.5
$\bar{1}$	1	1	5.27	5.27	65	53(−48)	4.8	5.9	4.2	4.2
0	0	1		4.51		90(90)		2.2	0.6[b]	0.6[b]
0	2	1		3.75		57(47)		2.1	0.2[b]	0.2[b]
$\bar{1}$	3	1	3.49	3.54	30	31(20)	2.1	3.1	2.3	2.2
$\bar{2}$	0	1	2.79	2.79	90	90(90)	4.7	4.7	4.7	4.7
0	4	1	2.72	2.70	43	41(28)	2.7	3.7	3.7	3.8
$\bar{2}$	2	1	2.57	2.58	78	81(−65)	2.2	2.0	1.8	2.0
$\bar{1}$	5	1	2.45	2.45	30	30(−13)	2.5	2.2	2.2	2.3
0	6	1	2.03	2.02	40	41(20)	2.2	1.6	1.6	1.7
$\bar{1}$	1	2	3.06	3.06	69	50(−46)	2.0	1.8	1.6	0.8[b]
$\bar{2}$	2	2	2.66	2.64	51	58(−48)	1.4	1.6	1.2	1.2
$\bar{2}$	4	2	2.18	2.18	54	45(−29)	2.0	1.6	1.6	1.7
$\bar{2}$	0	3	2.10	2.16	–[c]	90(90)	3.6	1.7	1.6	1.6
$\bar{2}$	2	3	2.10	2.00	–[c]	9(−2)	3.6	1.8	1.8	2.0
$\bar{1}$	1	3	1.93	1.93	90	85(73)	1.9	2.0	2.0	2.0

[a] Values in parenthesis are before correction for curvature of the Ewald sphere.
[b] Below threshold.
[c] Out of range in the area detector.

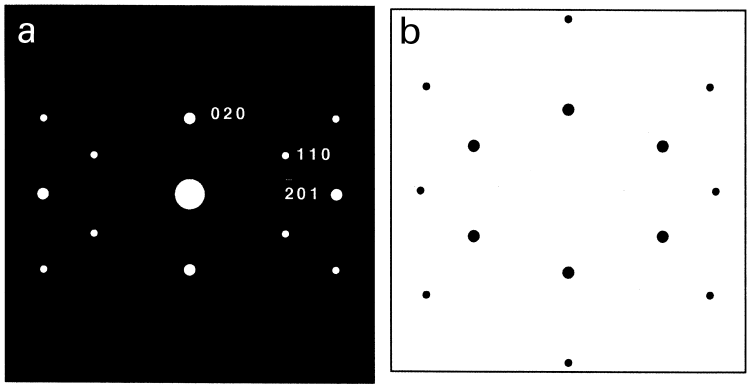

Fig. 4. (a) Reproduction of *hk*0 electron diffraction data for a single crystal of α-PPX (based on Ref. [13]; Fig. 2). (b) Schematic of the OD pattern for CN-PPX (Fig. 3(c)).

planar texture of the as-deposited film persists after drawing and annealing. The extent of this double orientation is apparent in the OD pattern (Fig. 3(c)), where we observe a number of arced reflections. The planar orientation is very high: the azimuthal half width of the reflection at $d = 6.76$ Å is only 13.7°. Thus, the drawn and annealed film has the texture of doubly oriented crystals, similar to the textures seen for α-PPX and PPX-F [4,18–20].

The OD pattern relates to the projection of the structure perpendicular to the chain axis, and is likely to define the reciprocal lattice parameters a^* and b^*. The broad strong equatorial reflection at $d = 3.96$ Å seen for the as-deposited film in Fig. 2(b), is resolved into two peaks in the OD pattern (Fig. 3(c)), indicating that both arise from planes inclined to the film surface. The reflection at $d = 6.76$ Å is meridionally disposed before and after drawing (Figs. 2(b) and 3(c)).

Fig. 4 compares schematics of the published electron diffraction pattern for a single crystal of α-PPX [10] and the OD pattern of CN-PPX in Fig. 3(c). The two patterns are seen to be very similar to each other in terms of the positions of the reflections, although the relative intensities are different. Based on analogy to the crystal structure of α-PPX, the meridional peak at $d = 6.76$ Å in Fig. 4(b) can be indexed as 200, and the off-equatorial peak as 110. The absence of 100 and 010 reflections strongly suggests that CN-PPX adopts a centered structure similar to that for α-PPX. The weak reflection at $d = 2.8$ Å on the equator in Fig. 4(b) can probably be indexed *hk*1 because it is seen on the first layer line in both the ND and TD patterns. The equivalent reflection for α-PPX was indexed as $\bar{2}01$ in Fig. 4(a). From these data, we can determine the monoclinic unit cell parameters to be $a = 5.96$ Å, $b = 13.52$ Å, $c = 6.48$ Å and $\beta = 135.9°$. The observed *d*-spacings are in good agreement with those calculated for this unit cell, as can be seen in Table 1. Systematic absences occur for $h + k =$ odd, consistent with centering in the *ab* face. With two monomers per unit cell, the theoretical density is 1.180 g/ml, which compares favorably with the observed density of 1.176 g/ml for the highly crystalline polymer.

Fig. 5 shows the intensity scans along the equator and first layer line as the specimen was rotated about the draw direction in 10° increments of ϕ ($\phi = 0$ and 90° correspond to the ND and TD orientation, respectively). The values of ϕ corresponding to the intensity maxima for the Bragg reflections were determined from these data, and those for layer lines 2 and 3, by interpolation, and are listed in Table 1 as $\phi_o(hkl)$. These are in good agreement with the calculated angles, $\phi_c(hkl)$, which were derived for the reciprocal lattice oriented as defined by the observed texture, allowing for the curvature of the Ewald sphere. As an example, the strong 020 and 110 reflections on the equator at $\phi_o = 10$ and 80° are predicted to occur at $\phi_c = 7$ and 84°, respectively (Fig. 5(a)). The 041, $\bar{2}01$, $\bar{2}21$ and $\bar{1}51$ reflections in the region of 2θ(31–37° are clearly separated at $\phi_o = 40$, 90, 80 and 30° (Fig. 5(b)) matching their predicted ϕ_c angles of 43, 90, 81 and 30°, respectively. We also observed traces of these *hk*1 reflections in the OD patterns (Fig. 3(c)), where the same positions are determined. Thus, the proposed unit cell reproduce not only the *d*-spacings, but also the coordinates of the lattice points in the reciprocal space. Note that the sign of ϕ cannot be determined because the reciprocal lattice and its mirror image are superimposed.

3.2. Molecular modeling

The conformation of the backbone is defined largely by the three torsion angles χ_1, χ_2 and χ_3. Molecular mechanics modeling predicts minimum energy conformations for C2/C2-, C2/C3-, C3/C2- and C3/C3-substituted dimers at $(\chi_1, \chi_2, \chi_3) = (88°, 179°, -81°)$, (90°,180°, − 90°), (83°, 188°, − 83°) and (82°,179°, − 90°), respectively. All of these are close to (90°,180°, − 90°), and the deviations result in only small decreases in energy, so the latter angles were used as the starting model in constructing the arrays of chains. The unsubstituted backbone has a center of symmetry at the center of the C7–C8 bond, which is taken as the origin.

The unit cell contains monomer units of two different chains. If we have a face centered lattice, one chain has its origin at 0,0,0 and the other is at $a/2, b/2, a\cos\beta/2$. (In

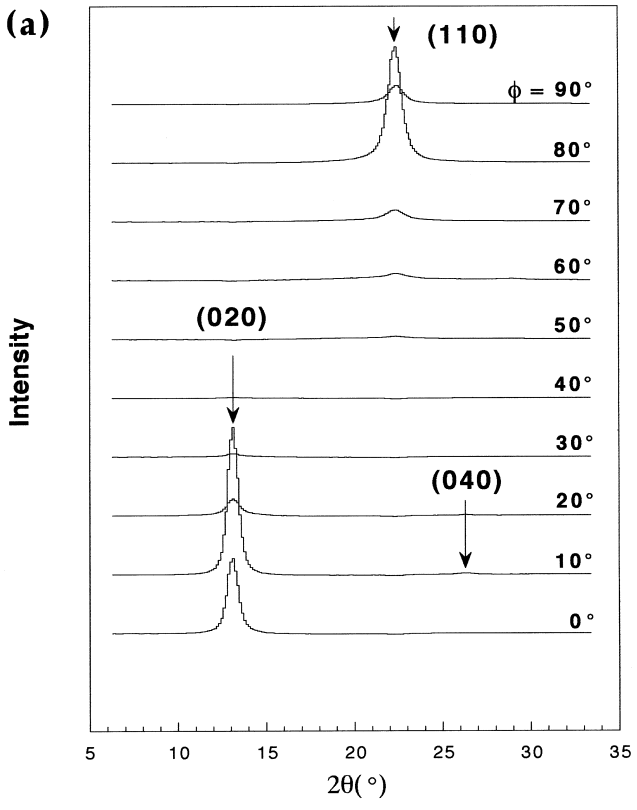

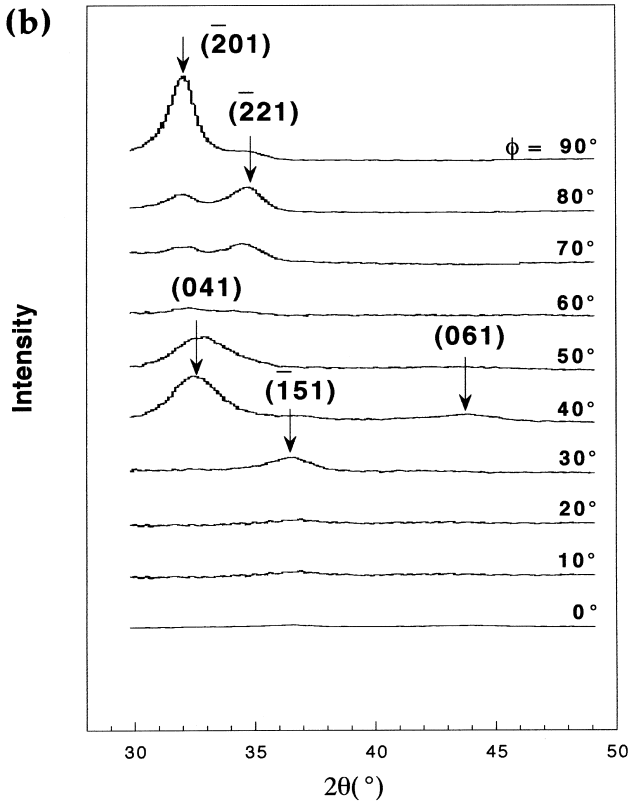

Fig. 5. Intensity scans along (a) the equator and (b) the first layer line recorded at 10° increment of ϕ.

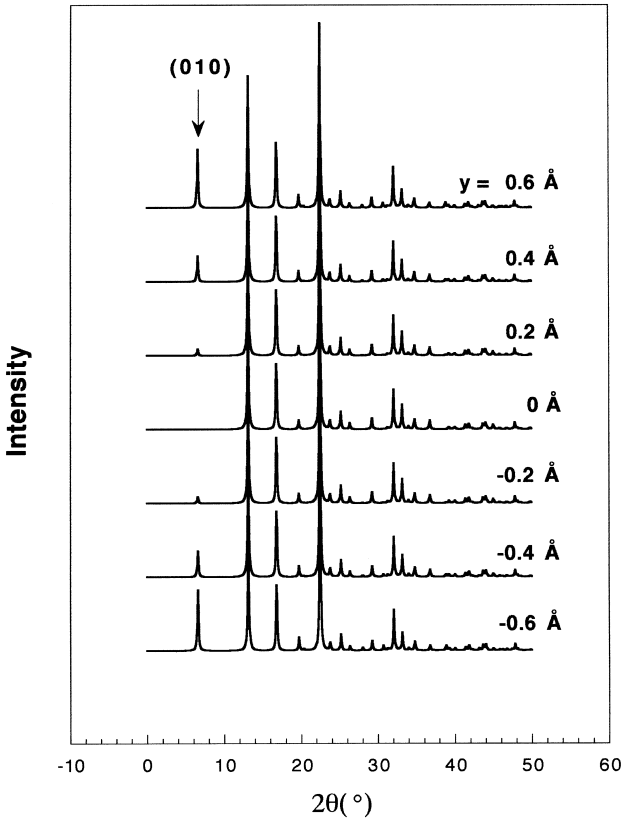

Fig. 6. Simulated powder diffraction patterns for model 2 for different shifts (in Å) of the center chain along the *b* axis.

order to confirm this restriction to C-centering, diffraction patterns were simulated for unit cell models in which the second chain is translated by small increments along *b* or *c*, is away from $a/2, b/2, a\cos\beta/2$. Fig. 6 shows the effects of small translations along *b* on the simulated diffraction pattern for an unoriented specimen. An unobserved 010 peak develops at $d = 13.52$ Å after a small shift of 0.2 Å because the centered symmetry is destroyed. Similarly small *c* axis displacements leads to several unobserved reflections notably on the first layer line, such as $\bar{1}01$ and $\bar{1}31$. Thus the origin of the second chain must be in the center of the *ab* face. The potential energy also has minimum when the second chain has its origin at the center of the *ab* face. Thus the modeling can be restricted to C-centered structures.

To examine the stereochemistry for the side chain packing, we constructed the four possible all-C2 substituted models, in which the symmetry operations (rotations) have the effect of placing the –CN group of the center chain at C2, C3, C5 or C6. The potential energy was calculated for an array of five chains of decamers for all four models, set up using the unit cell dimensions determined above. When the center chain is substituted at C2 or C3, the energy is −1.9 kcal/mol of monomer. In the case of C6-substitution, this increases to 3.0 kcal/mol of monomer; whereas for C5-substitution there is a large increase to

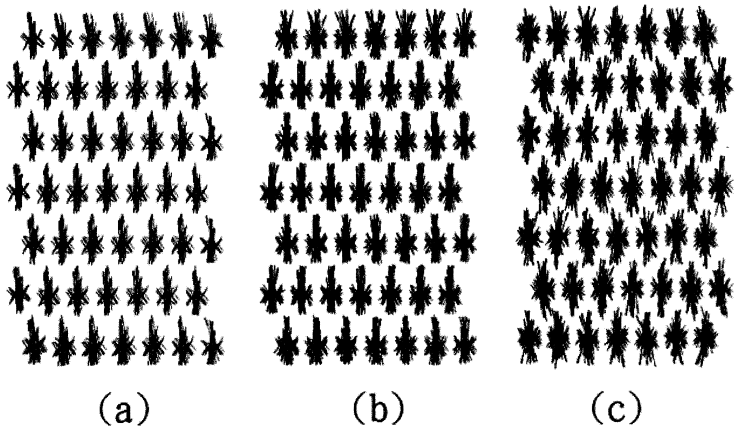

Fig. 7. *ab*-projections of the 7 × 7 arrays of decamers after energy minimization: (a) model 1; (b) model 2; and (c) model 3.

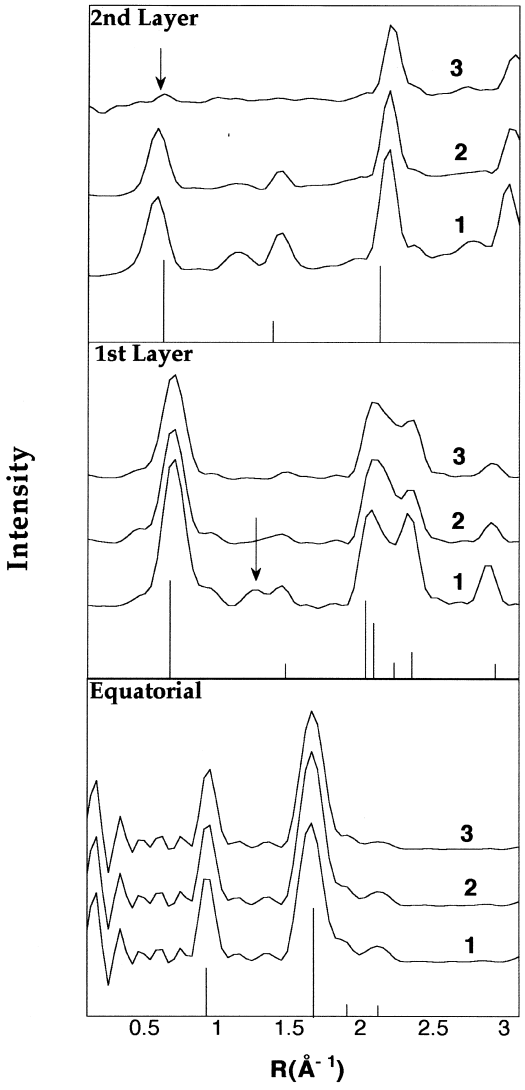

Fig. 8. Predicted intensity (plotted against *R*) on the equator and first two layer lines for models 1–3 after energy minimization. The vertical lines indicate the position and relative intensities of the observed reflection. The $\bar{1}12$ reflection discussed in the text is indicated by an arrow. Note that the relative intensities decrease considerably on going from the equator to the first and then to the second layer line.

540 kcal/mol due to serious overlap of the –CN groups. The energy for C5-substitution could be lowered by *b* translation of the central chain, which would eliminate the bad contact, but as shown above, this would eliminate the centered symmetry leading to an unobserved 010 reflection. However, it could also be eliminated by adjusting the backbone torsion angles near to this site, probably without major effect on the X-ray agreement.

Fig. 7 shows the *ab* projections of 7 × 7 arrays of decamers for models 1–3, following energy minimization. The three models have very similar energy: −5.78 kcal/mol of monomer for model 1 and −5.21 kcal/mol of monomer for models 2 and 3. The small differences indicate that there is no major problem in packing randomly substituted CN-PPX, i.e. changes in the local backbone conformation allow accommodation of the random side chains. However, it is apparent that the models become more distorted as the substitution becomes more random (all-C2 → C2/C3 → C2/C3/C5/C6). The extent of these distortions can be seen from the average torsion angles and their standard deviations: (χ_1, χ_2, χ_3) = (87 ± 2°, 179.5 ± 0.5°, −87 ±2°), (83 ± 8°, 174 ± 4°, −83 ± 8°) and (83 ± 10°, 174 ± 6°, −83 ± 10°) for models 1–3, respectively.

3.3. X-ray simulations

The X-ray scattering was simulated for the three models in two different ways. In the first, we used a unit cell approximation with different fractional occupancies for the –CN group. The second approach was to simulate the 2D X-ray fiber patterns for 7 × 7 arrays of chains.

Table 1 shows the structure amplitudes $|F_c(hkl)|$ for unit cell models 1–3. The crystallographic *R*-values are 0.26 for model 1, 0.21 for model 2 and 0.22 for model 3. Model 1 is inferior to the other two: the largest differences are for the unobserved 001 and 021 reflections, which are predicted to be observed for model 1. Models 2 and 3 are not significantly different in terms of *R*-value, and we cannot distinguish between them. Fig. 8 shows the intensity on the equator and first two layer lines in the simulated fiber

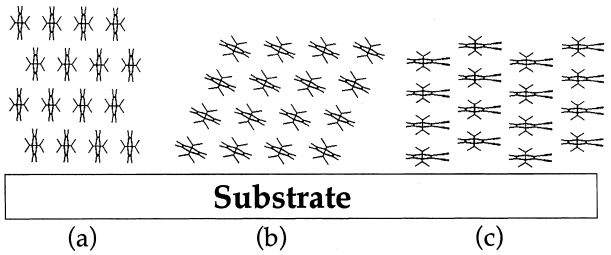

Fig. 9. Crystal lattices of the as-deposited polymers projected along the chain axes: (a) CN-PPX (model 2); (b) α-PPX; and (c) F-PPX.

patterns of the 7 × 7 arrays of decamers for models 1–3 after energy minimization. These data are very similar to those for the models before energy minimization, in that the small changes in backbone torsion angles do not have major effects. The simulation is in good qualitative agreement with the observed data (shown as the vertical lines), except for the $\bar{1}12$ reflection for model 3. This has medium intensity in the observed data, as is predicted for models 1 and 2, but it is very weak for model 3 (it would be unobservable above the background). This is the origin of the lower *R*-value for model 2, but better data would be necessary to resolve the question of a physical micro-structure in which all the –CN groups are directed to the same side of the molecule.

3.4. Discussion

Fig. 9 shows projections of the structures for α-PPX, CN-PPX and PPX-F, oriented as they are deposited on the substrate [4,10,13]. The preferred orientation in the as-deposited films is very different in the three polymers. For CN-PPX, the 100 planes are inclined parallel to the film surface, which means that the phenylene rings are almost parallel to the film surface (Fig. 9(c)). However, the phenylene rings are approximately perpendicular to the substrate surface in α-PPX (Fig. 9(a)) and have intermediate inclination in PPX-F (Fig. 9(b)). The orientation of the aromatic units in CN-PPX may be due to their larger planar area. CN-substitution also changes the polarity of the chain, which probably changes the interaction between the substrate and the growing chain. Another possible explanation is based on the different chain rigidities for the three polymers: the glass transition temperatures are 110°C for CN-PPX, >100°C for PPX-F and ~15°C for PPX [21]. However, we can only define the orientation of crystallites in the bulk film. Fig. 9 does not imply that we have any knowledge of the arrangement of the molecules at the interface with the substrate.

Table 2
Unit cell parameters, crystalline densities and pacing fraction for α-PPX, Cl-PPX, CN-PPX and PPX-F

	α-PPX [10]	Cl-PPX [13]	CN-PPX	PPX-F [4]
Dimensions (Å)				
a	5.92	5.92	5.96	5.36
b	10.64	12.80	13.52	5.92
c	6.55	6.55	6.48	6.57
Angles (°)				
α	90	90	90	97.0
β	134.7	135.0	135.9	63.1
γ	90	90	90	73.1
ρ (g/ml)	1.178	1.310	1.180	1.713
Packing fraction	0.70	0.65	0.65	0.66

Table 2 shows the unit cell parameters, densities and fractional packing volumes for α-PPX, Cl-PPX, CN-PPX and PPX-F. The *a* dimension is close to 5.9 Å for the first three polymers, so we can see that the changes in a' (i.e. in the *ab* projection) for PPX-F from 4.21 Å in these three polymers to 4.78 Å occurs in order to accommodate the larger fluorine atoms. The *b* dimension for α-PPX increases in Cl-PPX and CN-PPX in proportion to the size of the substituents. The β angle defines the staggering between the adjacent chains in the *a* direction and is almost the same (~135°) in the first three polymers: Cl- and CN-substitution does not effect on the staggering along the *a* direction because the substituents point along the *b* direction.

4. Conclusions

Films of CN-PPX (poly(cyano-*p*-xylylene)) prepared by vapor deposition polymerization process can have uniplanar orientation, depending on the temperature of the substrate. Films deposited at −35°C have almost no orientation, whereas those deposited at 40°C have a high degree of orientation, with the planes of the phenyl groups parallel to the substrate. This orientation is maintained after drawing the latter films 700% at 350°C, when the chains become aligned parallel to the direction of draw, leading to a mosaic texture of doubly-oriented crystals. Three dimensional wide angle X-ray data show that CN-PPX has a C-centered monoclinic unit cell with dimensions $a = 5.96$ Å, $b = 13.52$ Å, $c = 6.48$ Å and $\beta = 135.9°$.

Molecular modeling and X-ray simulations show that the crystal structure is similar to the α-form of the unsubstituted polymer, PPX. The unit cell is almost identical, except for the increased *b* dimension ($b = 10.64$ Å in PPX), which is due to the –CN substituents. The best agreement between the observed and calculated structure amplitudes ($R = 0.21$) is for a model where there is random substitution of the –CN groups on the phenylene ring.

References

[1] Gorham WF. J Polym Sci: A-1 1966;4(12):3027.
[2] Dabral S, Zhang X, Wu XM, Yang G-R, You L, Lang CI, Hwang K, Cuan G, Chiang C, Bakhru H, Olson R, Moore JA, Lu T-M, McDonald JF. J Vac Sci Technol 1993;B11:1825.
[3] Senkevich JJ, Desu SB. Appl Phys Lett 1998;72:258.
[4] Park S-Y, Blackwell J, Chvalun SN, Mailyan KA, Pebalk AV, Kardash IE. Macromolecules. In press.
[5] Plano MA, Kumar D, Cleary J. Mater Res Soc Symp Proc 1997;476:213.

[6] Beach WF, Lee C, Bassett DR, Austin TM, Olson R. Xylylene polymers, 2nd ed. Encyclopedia of polymer science and technology, vol. 17, 1989. p. 990–1025.
[7] Joesten BL. J Appl Polym Sci 1974;33:439.
[8] Nurmukhametov RN, Dyadyushkina SN, Nikolaev AA, Alexandrova LN, Gromov AV, Pebalk AV, Kardash IE. Polym Sci A 1993;35:433.
[9] Brown CJ, Farthing AC. J Chem Soc 1953;3270.
[10] Iwamoto R, Wunderlich B. J Polym Sci: Polym Phys Ed 1973;11:2403.
[11] Kubo S, Wunderich B. Makromol Chem 1972;162:1.
[12] Isoda S, Tsuji M, Ohara M, Kawaguchi A, Katayama K. Polymer 1983;24:1155.
[13] Isoda S, Kawaguchi A, Katayama K-I. J Polym Sci: Polym Phys Ed 1984;22:669.
[14] Yeh YL, Gorham WH. J Org Chem 1968;34(8):2366.
[15] Mailyan KA, Pebalk AV, Mishina EI, Kardash IE. Polym Sci A 1991;33:1530.
[16] Izumnikov AL, Achmeteva EI, Nikolaev AA, Kardash IE. Unpublished.
[17] Alexander LE. X-ray diffraction methods in polymer science. New York: Wiley-Interscience, 1969.
[18] Kubo S, Wunderlich B. J Polym Sci: Polym Phys Ed 1972;10:1949.
[19] Mailyan KA, Chvalun SN, Pebalk AV, Kardash IE. Polym Sci A 1992;34:761.
[20] Mailyan KA, Neverov VM, Pebalk AV, Chvalun SN, Kardash IE. Polym Sci A 1997;39:809.
[21] Kirkpatrick DE, Wunderich B. Makromol Chem 1985;186:2595.